



Calving Multiplier Effect Controlled by Melt Undercut Geometry

D. A. Slater^{1,2} , D. I. Benn¹ , T. R. Cowton¹ , J. N. Bassis³ , and J. A. Todd¹ ¹School of Geography and Sustainable Development, University of St Andrews, St Andrews, UK, ²School of Geosciences, University of Edinburgh, Edinburgh, UK, ³Department of Climate and Space Sciences and Engineering, University of Michigan, Ann Arbor, MI, USA**Key Points:**

- An elastic beam model is used to analyze calving driven by melt-undercutting at tidewater glaciers
- The presence of a calving multiplier effect is found to be sensitive to the shape of melt-undercutting
- The approach offers a promising route to parameterizing calving driven by melt-undercutting in large-scale ice sheet models

Supporting Information:

Supporting Information may be found in the online version of this article.

Correspondence to:D. A. Slater,
donald.slater@ed.ac.uk**Citation:**Slater, D. A., Benn, D. I., Cowton, T. R., Bassis, J. N., & Todd, J. A. (2021). Calving multiplier effect controlled by melt undercut geometry. *Journal of Geophysical Research: Earth Surface*, 126, e2021JF006191. <https://doi.org/10.1029/2021JF006191>

Received 30 MAR 2021

Accepted 8 JUN 2021

Abstract Quantifying the impact of submarine melting on calving is central to understanding the response of marine-terminating glaciers to ocean forcing. Modeling and observational studies suggest the potential for submarine melting to amplify calving (the calving multiplier effect), but there is little consensus as to under what conditions this occurs. Here, by viewing a marine-terminating glacier as an elastic beam, we propose an analytical basis for understanding the presence or absence of the calving multiplier effect. We show that as a terminus becomes undercut it becomes more susceptible to both serac failure (calving only of ice that is undercut, driven by vertical imbalance) and rotational failure (full-thickness calving of ice behind the grounding line, driven by rotational imbalance). By deriving analytical stress thresholds for these two forms of calving, we suggest that the dominant of the two calving styles is determined principally by the shape of melt-undercutting. Uniform undercutting extending from the bed to the waterline promotes serac failure and no multiplier effect, while glaciers experiencing linear undercutting that is greatest at the bed and zero at the waterline are more likely to experience rotational failure and a multiplier effect. Our study offers a quantitative framework for understanding where and when the calving multiplier effect occurs, and, therefore, a route to parameterizing the effect in ice sheet-scale models.

1. Introduction

Calving and submarine melting are key forms of mass loss at glaciers that terminate in water. For the Greenland ice sheet, the combination of calving and submarine melting is the largest source of mass loss in a typical year (van den Broeke et al., 2016) and an increase in calving and submarine melting is responsible for half of Greenland's 1992–2018 sea level contribution of 10.8 mm (The IMBIE Team, 2020). Given the likelihood of continuing global ice mass loss over the coming decades and centuries (Goelzer et al., 2020; Hock et al., 2019; Seroussi et al., 2020), understanding calving and submarine melting and their interplay, and ensuring their faithful representation in models are high priorities.

Calving occurs in many styles depending on the geometry of the ice body and can take the form of frequent small events or infrequent large events (Åström et al., 2014; Benn et al., 2007). Calving may be driven purely by geometric effects or may be sensitive to external influences such as surface melt, ice mélange or submarine melting (Benn, Cowton, et al., 2017; Catania et al., 2020). The focus of this study is on glaciers with grounded termini and on the interaction of calving with submarine melting. Submarine melting removes ice from the submerged portion of the terminus, and, depending on the distribution of melting, can give rise to termini that are preferentially undercut at depth, at the water surface or in confined chimneys above subglacial channels (Fried et al., 2019; Rignot et al., 2015; Slater et al., 2018; Sutherland et al., 2019; Wagner et al., 2019). In turn, undercutting may influence calving through (a) changing buoyant forces at the terminus giving rise to rotational or vertical imbalances (Hanson & Hooke, 2000; Hughes, 1992), (b) the removal of lateral support provided to the glacier by side walls (Cowton et al., 2019) or (c) the removal of basal friction resulting in ice flow acceleration and increased stresses within the ice (Morlighem et al., 2016). The potential for submarine melting, through each and any of these processes, to drive calving at many times the rate of melting has become known as the “calving multiplier effect” (Benn, Astrom, et al., 2017; Ma & Bassis, 2019; O’Leary & Christoffersen, 2013).

© 2021. The Authors.

This is an open access article under the terms of the [Creative Commons Attribution License](https://creativecommons.org/licenses/by/4.0/), which permits use, distribution and reproduction in any medium, provided the original work is properly cited.

Due to coarse model resolution and a lack of process understanding and suitable parameterizations, the representation of the impact of submarine melting on calving in ice sheet-scale models is currently limited. In a recent leading sea level projection exercise, most ice sheet models did not have sufficient resolution to resolve calving and relied on a pragmatic but heavy-handed parameterization for glacier retreat (Goelzer et al., 2020; Slater et al., 2019). Only the more advanced models resolved calving and submarine melting (Aschwanden et al., 2019; Morlighem et al., 2019), but even these state-of-the-art approaches do not, explicitly at least, account for the first two of the three influences of submarine melting on calving described above. Because resolving all of the relevant processes is beyond current computational capabilities, work toward calving parameterizations is of great importance.

Observational constraints on the impact of submarine melting on calving are hard to come by due to the difficulty and danger of measuring submarine melting, the shape of the terminus beneath the water and the magnitude of calving events. The link between submarine melting and calving has, therefore, often been inferred from large-scale remote observations connecting glacier retreat to ocean warming (e.g., Straneo & Heimbach, 2013). At the glacier scale, Luckman et al. (2015) found a significant relationship between near-glacier water temperature and frontal ablation rate at three tidewater glaciers in Svalbard, strongly suggestive of a tight relationship between submarine melting and calving. Bartholomaeus et al. (2013) and How et al. (2019) have similarly argued on observational grounds for calving being paced by melt-undercutting. At each of the glaciers considered in these studies, however, most of the calving was small scale, high frequency events above the water line suggesting the calving rate would be equal to the submarine melt rate. A significant calving multiplier effect has not, to our knowledge, been conclusively observed.

Much of our knowledge on the calving multiplier effect, therefore, comes from models, yet such studies are equivocal on the impact of submarine melting on calving. Using flowband simulations in Elmer/Ice, Cook et al. (2014), Todd and Christoffersen (2014), and Krug et al. (2015) all argued for a limited impact of submarine melting on calving, while Mercenier et al. (2020) suggest that increased melting can, in fact, decrease total mass loss. Vallot et al. (2018), Todd et al. (2018), Todd et al. (2019), and Cowton et al. (2019) have argued for a nuanced effect of submarine melting on calving, in which melt is important to the seasonal details of the calving, or is important depending on the magnitude and distribution of melting. Three recent studies very explicitly simulate a calving multiplier effect. Ma and Bassis (2019) used flowband simulations, accounting for damage evolution and both tensile and shear failure, to find a calving multiplier effect for certain melt rates and undercut shapes. Benn, Astrom, et al. (2017) identified a calving multiplier effect for certain water depth, ice thickness and undercut length combinations. In simulations of Bowdoin Glacier, van Dongen et al. (2020) recently argued for a multiplier effect for certain distributions of submarine melting. The latter two studies used a discrete particle model from which calving styles appear naturally without the need to impose modes of failure.

The emerging picture then, is that the calving multiplier effect does prevail in some situations, depending on the topographic regime of the glacier, the relative magnitude of the submarine melt rate and ice velocity, the distribution of submarine melting, or the water depth and ice thickness. As such, there is little consensus on the impact of submarine melting on calving, precluding the development of a unifying parameterization for incorporating this essential link into ice sheet-scale models. Here, we suggest framing the presence or absence of the calving multiplier effect based on a simple thresholding of the tensile and shear stresses obtained when considering the glacier as an elastic beam subject to a torque and shear at one end. The basic idea is that a multiplier effect is active if an undercut can stably grow sufficiently large that the torque exerted on the terminus results in a bending moment in the ice that exceeds a threshold value. If, instead, the undercut ice calves through shear/serac failure before the bending moment threshold is reached, no multiplier effect is observed. The elastic beam approach we take offers a promising analytical route toward parameterizing the presence or absence of the calving multiplier effect in ice sheet-scale models.

2. Methods

2.1. Elastic Beam Theory

The fundamental tool used in this study is elastic thin beam theory and is not new to glaciology, having been extensively used to study buoyant flexure of ice shelves (e.g., Mosbeux et al., 2020; Sayag & Worster, 2011;

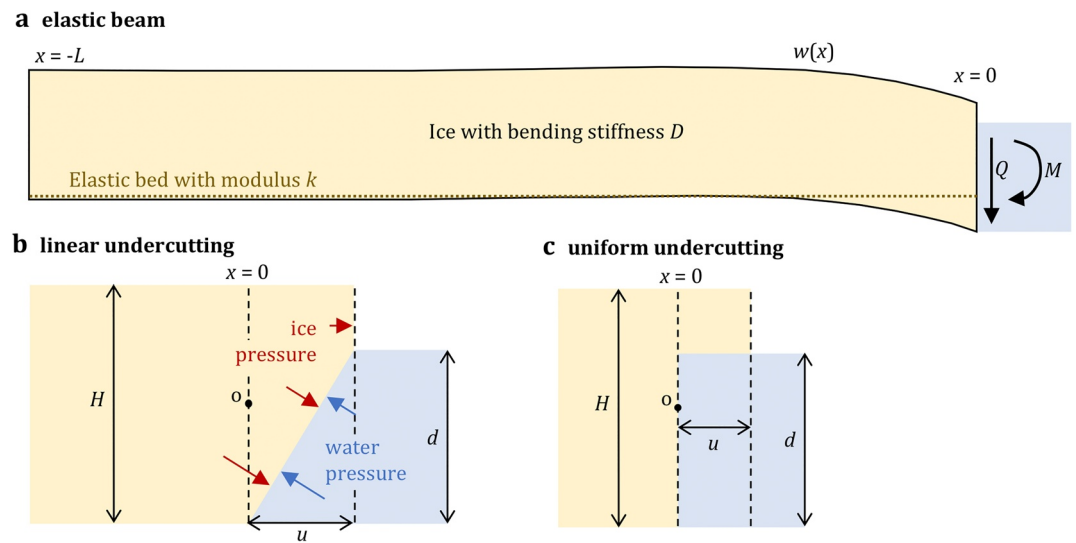


Figure 1. Schematic of the glacier and terminus geometry. (a) A tidewater glacier considered as an elastic beam, with ice/water pressure and undercutting exerting shear and torque on the terminus such that the glacier flexes. The flat profile of the elastic bed shows its position before loading by the glacier. Note that this illustration is vertically exaggerated. The detail at the terminus is shown for the (b) linearly undercut geometry and (c) uniformly undercut geometry. All variables are defined in the text.

Sergienko, 2010; Vaughan, 1995) and tidewater glaciers (Wagner et al., 2016). It has not, however, been used to model the stress response of a tidewater glacier to melt-undercutting at its terminus. Beam theory describes the shape and stress response of an elastic beam to loading along its length or at one end. Let the glacier (i.e., beam) flow from left to right with coordinate x measuring the along flow distance and let the ice divide and grounding line be at $x = -L$ and $x = 0$, respectively (Figure 1a). The glacier has a constant ice thickness H and a constant bending stiffness $D = EH^3/12(1 - \nu^2)$, where E is the elastic modulus and ν is Poisson's ratio. The ice has density $\rho_i = 910 \text{ kg m}^{-3}$, is subject to gravity $g = 9.81 \text{ m s}^{-2}$ and rests on a Winkler foundation: that is, a flat elastic bed of stiffness k . The glacier surface elevation from the ice divide to the grounding line, $w(x)$, is then given by (e.g., Sayag & Worster, 2011)

$$Dw'''' + kw = -\rho_i gH \quad (1)$$

where the primes denote derivatives with respect to x . All solutions to Equation 1 used in this study are obtained analytically, and, except where stated otherwise, we take $E = 1 \text{ GPa}$ and $\nu = 0.3$. The bed stiffness is not well constrained by observations, though Sayag and Worster (2013) have argued that values of approximately $k = 1 \text{ MPa m}^{-1}$ to 1 GPa m^{-1} are appropriate for deformable glacial till at the bed. Unless stated otherwise, we assume a value $k = 1 \text{ MPa m}^{-1}$, appropriate for soft till, as has been inferred to persist beneath Greenland's largest tidewater glaciers (e.g., Shapero et al., 2016).

The glacier terminates in water of depth d and density $\rho_w = 1,030 \text{ kg m}^{-3}$ and the terminus of the glacier is taken to be vertical or undercut. Although none of the mathematical set-up is specific to an undercut shape, we will in the results section consider two undercut shapes: a linear undercut when undercutting increases linearly from zero at the waterline to a length of u at the bed (Figure 1b) and a uniform undercut when all of the submerged ice is undercut to a length u (Figure 1c). This undercutting and the imbalance between ice and water pressure at the terminus impose a torque and shear on the glacier that are represented in beam theory by boundary conditions.

The use of a thin beam model (Equation 1) is an approximation to the full two-dimensional flowline problem. The thin beam approach is, in general, appropriate when the ice thickness is not large compared to the flexural wavelength of the glacier. In the present application, this is certainly the case for the thinner glaciers considered ($H \sim 100 \text{ m}$), but for thick glaciers ($H \sim 900 \text{ m}$) additional effects beyond the thin beam model may become more important. We expect, however, that these additional effects will make

quantitative rather than qualitative differences to our results; that is, the use of a more complex model would change some of the numbers, but would not change the findings or conclusions. The great benefit of using a thin beam model is the opportunity to make analytical progress on a topic that is dominated by models of high complexity and we therefore consider its use to be justified for the present application.

From the outset it is also important to note that our analysis considers a glacier flowline (Figure 1) and, therefore, neglects across-glacier variability in stress and terminus shape. As such, our results will be most appropriate where the glacier has a width that is large compared to the ice thickness and where undercutting extends across a broad swath of the terminus. Because observations of the submerged shape of calving fronts do, however, show significant across-glacier variability (Fried et al., 2019), including localized undercut chimneys, the flowline nature of our analysis is a limitation that should be borne in mind throughout. We nevertheless consider it an important step toward understanding the impact of submarine melting on calving, and particularly toward parameterizing this process in ice sheet models.

2.2. Boundary Conditions

Solution of Equation 1 requires four boundary conditions that, for a glacier that is undercut at its terminus, are taken as $w(-L) = -\rho_i g H / k$, $w'(-L) = 0$, $w''(0) = M / D$, and $w'''(0) = Q / D$. The first two conditions ensure that far inland from the grounding line, the weight of the glacier is fully supported by the bed and the surface elevation is flat. Note that the solutions presented later are given in the limit $L \rightarrow -\infty$. The third condition imposes a torque at the grounding line that arises from the imbalance between ice and water pressure (Figure 1b) and the fourth condition imposes a shear at the grounding line that is required to support the weight of undercut ice beyond the grounding line (Figures 1b and 1c). Note that the undercut region is not modeled explicitly; rather, the effect of the undercut region is imposed through the torque and shear boundary conditions applied at the grounding line.

The depth-integrated torque at the grounding line, M , is evaluated on the neutral plane of the beam (i.e., halfway between the bed and ice surface) and is defined as $M = \int F \times r \, dr$. Here, F is the net force resulting from the ice and water pressure, r is the vector from the neutral plane at the grounding line (point “o” on Figures 1b and 1c) to the terminus and the integral runs over the subaerial and submerged interfaces of the terminus (Figure 1b). Note that the depth-integrated torque acts to rotate the terminus top-forwards into the ocean when $M < 0$ and bottom-forwards into the ocean when $M > 0$. The depth-integrated shear at the grounding line, Q , is calculated as the difference between the weight of ice beyond the grounding line and the weight of water that it displaces.

2.3. Solution of Elastic Beam Theory

The elastic beam model (Equation 1) has an analytical solution given by

$$w = \frac{\lambda^2}{2D} \left[(M - Q\lambda) \cos\left(\frac{x}{\lambda}\right) + M \sin\left(\frac{x}{\lambda}\right) \right] \exp\left(\frac{x}{\lambda}\right) - \frac{\rho_i g H}{k} \quad (2)$$

in which $\lambda = \left(\frac{4D}{k}\right)^{1/4} = \left[\frac{EH^3}{3k(1-\nu^2)}\right]^{1/4}$ is the characteristic length scale that controls how far up-glacier the terminus boundary conditions are felt. For the adopted values of the ice and bed modulus, $\lambda = 450$ m when the ice thickness is $H = 500$ m. Note that the term in the fully general solution that is proportional to $\exp\left(-\frac{x}{\lambda}\right)$ vanishes in the limit $L \rightarrow -\infty$ assumed here. The longitudinal stress on the top surface of the glacier, σ_r , is given by (e.g., Wagner et al., 2016)

$$\sigma_r = -\frac{6D}{H^2} w'' = \frac{6}{H^2} \left[(M - Q\lambda) \sin\left(\frac{x}{\lambda}\right) - M \cos\left(\frac{x}{\lambda}\right) \right] \exp\left(\frac{x}{\lambda}\right) \quad (3)$$

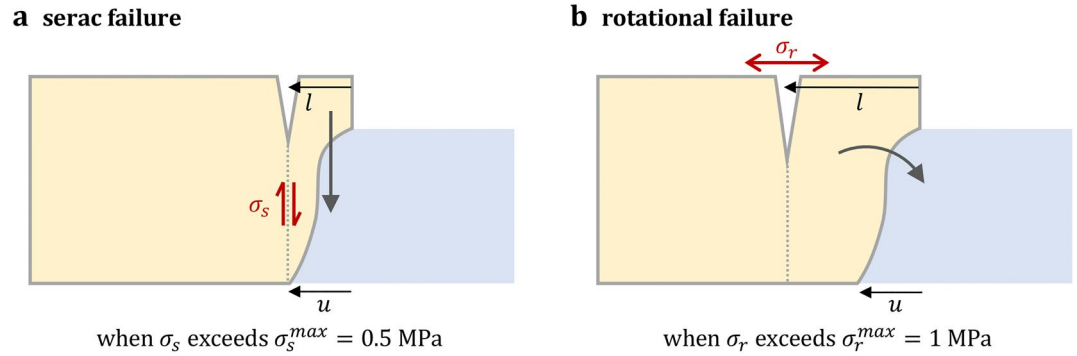


Figure 2. Schematic of calving styles considered. (a) Serac failure is imposed when the depth-mean shear stress at the grounding line, σ_s , exceeds a threshold value taken as $\sigma_s^{max} = 0.5$ MPa. (b) Rotational failure is imposed when and where the longitudinal stress at the glacier surface, σ_r , has a maximum value that exceeds $\sigma_r^{max} = 1$ MPa. As a glacier becomes progressively more undercut at the terminus, the dominant calving-style is determined by which of these two thresholds is reached first. The undercut shape shown in these schematics is non-specific; in this study we consider only linear and uniform undercutting (Figure 1).

Lastly, the depth-mean shear at the grounding line, σ_s , can be obtained by dividing the depth-integrated shear by the grounding line ice thickness H_{gl} :

$$\sigma_s = Q / H_{gl} \quad (4)$$

2.4. Calving Criteria

With the described framework, we are able consider two calving styles: serac failure and rotational failure (Figure 2). Rather than adopting a scheme to calculate crevasse depth (e.g., Benn et al., 2007), we assume that full-depth crevassing and calving occurs when the shear or tensile stresses exceed a threshold value.

Serac failure involves calving only of ice that is undercut and results from high shear stress (Figure 2a). It can be shown that the highest shear stress at any point along the undercut ice is almost always at the grounding line (supporting information) and so serac failure is most likely to occur at the grounding line itself. We impose serac failure (Figure 2a) when the depth-mean shear stress at the grounding line, σ_s , exceeds a threshold value that is taken as $\sigma_s^{max} = 0.5$ MPa (e.g., Ma & Bassis, 2019). An alternative serac failure mechanism involving downward bending of the cantilever beam formed by uniform undercutting is considered in supporting information but does not give significantly different results.

Rotational failure is calving resulting from a high bending moment in the ice (Figure 2b). This bending moment is a response to the torque and shear exerted at the terminus and results in tensile and compressive stresses on the top and bottom of the glacier, respectively. We impose rotational failure (Figure 2b) when the longitudinal stress, σ_r , at any point on the top surface of the glacier exceeds a threshold value that is taken as $\sigma_r^{max} = 1$ MPa (e.g., Ultee et al., 2020). Failure is assumed to occur at the surface stress maximum, which from Equation 3 is located at the point x_0 given by

$$\tan\left(\frac{x_0}{\lambda}\right) = \left(\frac{2M}{Q\lambda} - 1\right)^{-1} \quad (5)$$

and the maximum value can be obtained by substituting x_0 into Equation 3. Note that due to the boundary conditions (Section 2.2) and because for vertical or undercut ice the depth-integrated shear Q is always zero or positive, the maximum of the longitudinal stress on the top surface of the glacier is always located at or upstream of the grounding line. Rotational failure, therefore, involves full-thickness calving of ice upstream of the grounding line.

For melt-undercutting to be the process driving calving, we require the glacier to be stable to calving when the front is vertical. Large glaciers terminating in shallow water are unstable to ice cliff failure before undercutting and are, therefore, not observed in reality (Bassis & Walker, 2012). As such, in this study we only consider glaciers that are stable to ice cliff failure according to the metric of Bassis and Walker (2012), which restricts the possible ice thickness and water depth combinations to those that satisfy

$$\frac{1}{4} \rho_i g H \left[1 - \frac{\rho_w}{\rho_i} \left(\frac{d}{H} \right)^2 \right] < \sigma_s^{max} \quad (6)$$

For a given ice thickness, this condition imposes a minimum water depth on the glaciers we consider. For example, if $H = 500$ m, the water depth d must exceed 350 m. Although ice thicknesses up to 1,900 m are allowable under Equation 6, with Greenlandic tidewater glaciers in mind we will below consider a maximum ice thickness $H = 900$ m.

For a glacier that is stable when the front is vertical, we define the dominant calving-style by which failure threshold (serac or rotational) is reached first as the terminus becomes progressively more undercut. If the calving length, l , is the distance from the most advanced part of the glacier to the calving position and u is the undercut length at the grounding line (Figure 2), then we define the calving multiplier as $\beta = l/u$. Serac failure by definition occurs at the grounding line, hence $l = u$ and $\beta = 1$, and there is no multiplier effect under serac failure. Rotational failure occurs upstream of the grounding line, hence $l > u$ and $\beta > 1$, and there is a multiplier effect. The presence of a multiplier effect, therefore, depends on the dominant calving-style, which is now analyzed using elastic beam theory and the described framework.

3. Results

3.1. Serac Failure

Because the depth-mean shear stress at the grounding line is entirely determined by the geometry of the undercut, serac failure can be analyzed independently of beam theory. The depth-mean shear stress (i.e., the depth-mean of σ_{xz}) at the grounding line is given by

$$\sigma_s = \frac{Q}{H} = \rho_i g u \left[1 - \frac{d}{2H} \left(1 + \frac{\rho_w}{\rho_i} \right) \right] \quad (7)$$

for a linear undercut and $\sigma_s = Q/(H - d) = \rho_i g u$ for a uniform undercut, with details of the calculation given in supporting information. For linear undercutting, the shear stress at the grounding line increases with greater undercutting because there is more ice beyond the grounding line that must be supported (Figure 3a). The shear stress decreases with deeper water because more of the weight of ice beyond the grounding line is hydrostatically compensated (Figure 3a). For uniform undercutting, the shear stress similarly increases with greater undercutting, but is independent of the water depth because none of the undercut ice is supported by the ocean at all (Figure 3b).

The imposition of the shear stress threshold for failure gives a critical undercut length, u_s , at which serac failure occurs, given from Equation 7 as

$$u_s = \frac{\sigma_s^{max}}{\rho_i g} \left[1 - \frac{d}{2H} \left(1 + \frac{\rho_w}{\rho_i} \right) \right]^{-1} \quad (8)$$

for linear undercutting, or $u_s = \sigma_s^{max} / \rho_i g$ for uniform undercutting. As would be expected from Figures 3a and 3b, the critical undercut length increases sensitively with the water depth for linear undercutting but is independent of the water depth for uniform undercutting (Figure 3c). With $\sigma_s^{max} = 0.5$ MPa, serac failure occurs at an undercut of $u_s = 56$ m for uniform undercutting regardless of water depth, but not until an undercut of $u_s = 220$ m for linear undercutting when the water depth fraction, d/H , is 0.7.

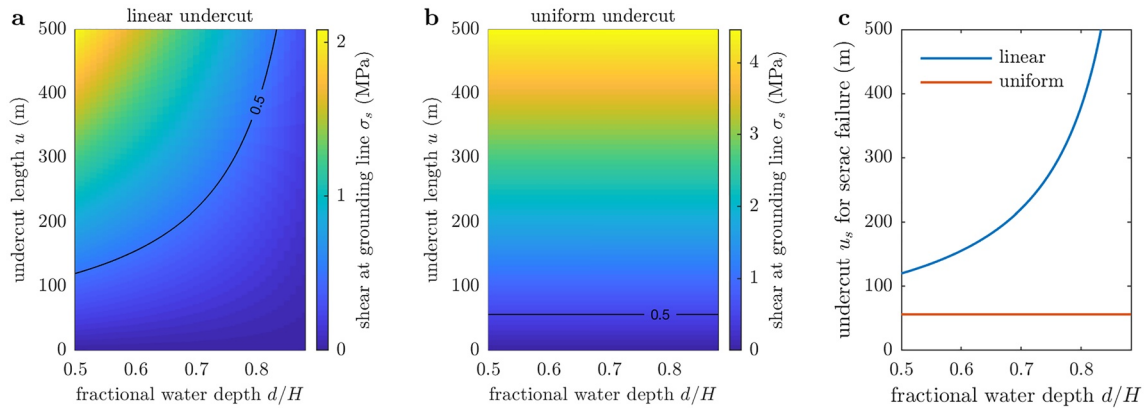


Figure 3. (a) Depth-mean shear stress at the grounding line for linearly undercut ice as a function of fractional water depth and undercut length. The fractional water depth ranges from $d/H = 0.5$ to $d/H = 0.88$ (flotation). The black contour shows the failure threshold $\sigma_s^{max} = 0.5$ MPa. (b) The equivalent depth-mean shear stress at the grounding line for uniformly undercut ice. Note the different color scale compared to (a). (c) The critical undercut length, u_s , at which the depth-mean grounding line shear reaches the threshold value ($\sigma_s = \sigma_s^{max}$). This is the undercut length at which serac failure occurs.

Note that these undercutting thresholds assume fully intact ice at the grounding line of thickness H in the linearly undercut case and $H - d$ in the uniformly undercut case. If, instead, the glacier has surface crevasses over the grounding line such that the remaining intact ice thickness is a fraction f of the fully intact ice thickness, then the undercut length for serac failure (Figure 3c; Equation 8) is reduced by a factor f . For the examples just given, if $f = 0.5$, so that the crevasse depth is $(H - d)/2$ in the uniformly undercut case and $H/2$ in the linearly undercut case, then serac failure would occur at an undercut of $u_s = 28$ m for uniform undercutting and $u_s = 110$ m for linear undercutting when the water depth fraction is 0.7.

3.2. Depth-Integrated Torque on the Calving Front

Analyzing rotational failure is more complex, but before looking at beam theory it is instructive to first examine the depth-integrated torque, M , exerted on the calving front by ice and water pressure. We here analyze only the linear undercut case, but emphasize that the uniformly undercut case is similar (supporting information). The depth-integrated torque for the linearly undercut case is

$$M = \frac{1}{12} \rho_i g H^3 \left[1 - \frac{\rho_w}{\rho_i} \left(3 \frac{d^2}{H^2} - 2 \frac{d^3}{H^3} \right) - 6 \left(1 - \frac{2d}{3H} - \frac{1}{3} \frac{\rho_w}{\rho_i} \frac{d}{H} \right) \frac{u^2}{H^2} \right] \quad (9)$$

with details of the calculation given in supporting information.

First, for a given water depth fraction d/H , the depth-integrated torque always decreases as the length of the undercut increases (Figure 4a). Thus, undercutting always increases the propensity of the terminus to tip top-forwards into the ocean (Figure 4a). Second, for a vertical ($u/H = 0$) or slightly undercut ($u/H = 0.25$) terminus, the depth-integrated torque decreases as the water depth increases, because the greater water pressure acts to tip the terminus top-forwards (Figure 4b). In particular, for a vertical terminus, the depth-integrated torque on the calving front acts to tip the terminus top-forwards only when the fractional water depth d/H exceeds 0.78. For deep undercutting ($u/H = 0.5$), however, the depth-integrated torque increases with deeper water because the water increasingly supports the weight of the undercut ice (Figure 4b). Viewing the depth-integrated torque as a function of both the water depth and undercut length shows that for shallow water and shallow undercutting, the torque is positive and, therefore, acts to tip the terminus bottom-forwards (Figure 4c). As an aside, when sufficiently large this positive torque has been implicated in ice cliff failure (Hanson & Hooke, 2000), though in this study we use a longitudinal stress-based ice cliff failure criteria (Equation 6). For deep water or deep undercutting, the torque is negative and acts to tip the terminus top-forwards (Figure 4c).

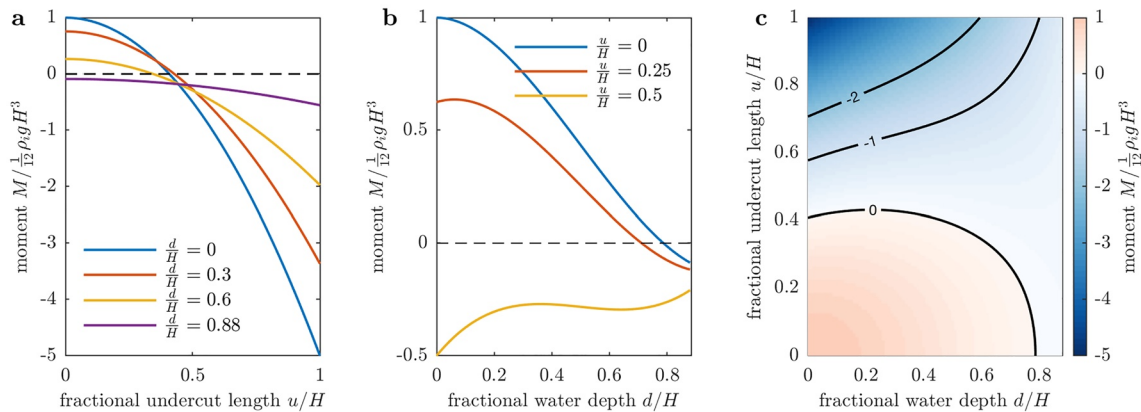


Figure 4. The rotational moment acting on the calving front as a result of hydrostatic ice and water pressure and linear undercutting. Negative values of the rotational moment indicate a calving front that wants to tip top-forwards into the water. (a) The moment as a function of undercutting for various water depths. The moment is normalized by $\frac{1}{12} \rho_i g H^3$, which is its value when the calving front is vertical ($u/H = 0$) and there is no water ($d/H = 0$). (b) The normalized moment as a function of water depth for three undercutting scenarios. (c) The normalized moment as a function of both water depth and undercutting.

3.3. Elastic Beam Solutions

Some example solutions of the elastic beam model (Equations 2 and 3) are shown in Figure 5. For a vertical terminus, there is no shear acting on the front, and if in addition the water depth is sufficiently small, the torque on the terminus acts to tip it bottom-forwards and so the glacier flexes upwards at the front (Figure 5a) and the resulting longitudinal stress on the glacier surface is compressive close to the terminus (Figure 5b). For deeper water (but still a vertical terminus), the torque acts to tip the front top-forwards and so the glacier flexes downwards at the front and the surface stress is tensile, with a maximum at the grounding line. Once undercutting is imposed, there is both a torque and a shear acting on the terminus. The glacier increasingly flexes downwards at the terminus (and upwards some distance upstream), the surface stress increases in magnitude and the surface stress maximum is upstream of the grounding line (Figure 5). The distance upstream to the stress maximum is largely controlled by the characteristic length λ .

An important distinction is between scenarios where the glacier flexes upwards or downwards at the terminus, as this determines whether the surface stress is compressive or tensile close to the terminus (e.g., Figure 5). Based on the analytical solution (Equation 2) it can be shown that the glacier flexes downwards when $2M < Q\lambda$. If the terminus is vertical (so that there is no shear and $Q = 0$), then the glacier flexes downwards when the torque acts to tip the glacier top-forwards ($M < 0$). If the torque acts to tip the glacier

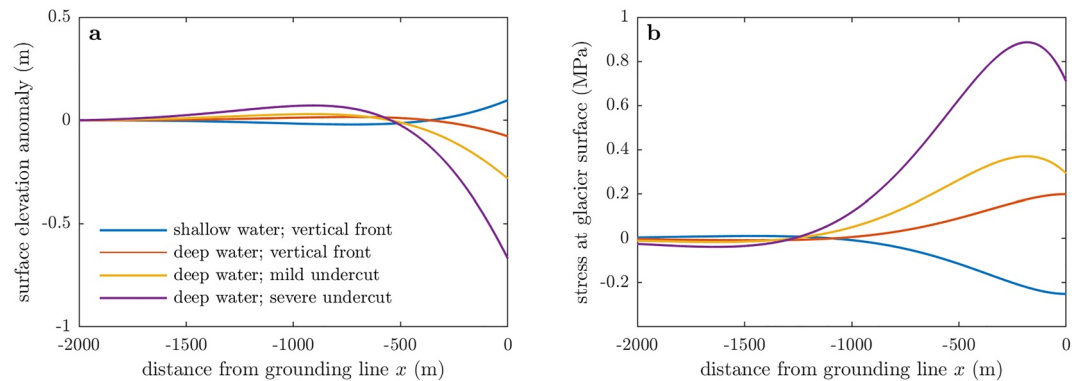


Figure 5. Example solutions of elastic beam model for various water depth and linear undercut scenarios, showing (a) glacier surface elevation and (b) longitudinal stress at the glacier surface. All solutions have ice thickness $H = 500$ m. Examples shown are blue: shallow water $d = 350$ m and a vertical front $u = 0$ m, red: deep water $d = 442$ m (floatation) and a vertical calving front $u = 0$ m, yellow: deep water $d = 442$ m and mild undercut $u = 150$ m, purple: deep water $d = 442$ m and severe undercut $u = 350$ m.

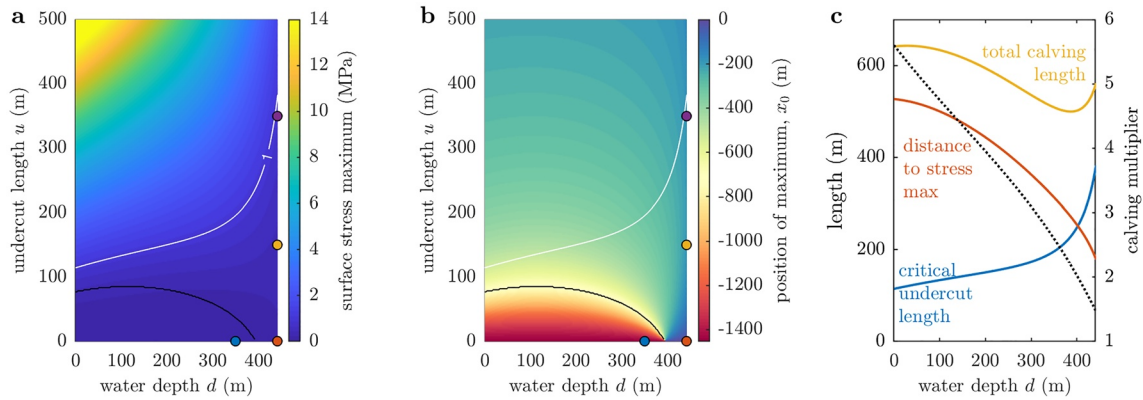


Figure 6. (a) Surface longitudinal stress maximum and (b) location of maximum using the elastic beam model for an ice thickness $H = 500$ m and variable water depth and linear undercut length. The white contours on (a) and (b) show the failure threshold $\sigma_r^{max} = 1$ MPa that also defines the critical undercut length. The colored markers on (a) correspond to the examples shown in Figure 5. The black line separates glaciers that flex upwards (below the line) and downwards (above the line) at the terminus. (c) Left axis: the critical undercut length u_r (blue) at which the surface stress maximum hits the threshold value and rotational failure occurs, together with the calving position $|x_0|$ (red) and the total calving length $l = u_r + |x_0|$ (yellow). Right axis and black dotted line: the calving multiplier $\beta = l/u_r$.

bottom-forwards ($M > 0$), it is still possible for the glacier to flex downwards provided undercutting results in sufficient shear on the terminus to pull it downwards. Thus, the flexure of the glacier and the nature of the surface stress is determined by both the torque and the shear acting on the terminus, which are in turn functions of the ice thickness, water depth, undercut length and undercut shape.

3.4. Rotational Failure

For an ice thickness $H = 500$ m but variable water depth and linear undercut length, the magnitude and position of the stress maximum are given through Equation 5 and shown in Figure 6. The magnitude of the stress maximum increases with the degree of undercutting (Figure 6a, see also Figure 5b), and except for very large undercut lengths, also increases with the water depth. The position of the stress maximum (x_0 , which is negative because it is upstream of the grounding line) is furthest behind the grounding line at small water depths and undercut lengths (Figure 6b), but because the magnitude of the stress maximum in this region of the parameter space is small (Figure 6a), calving is unlikely to occur. The position of the stress maximum moves closer to the grounding line as the water depth is increased. When the front is vertical and the glacier is flexing downwards at the terminus, the maximum is located at the grounding line.

We have suggested imposing rotational failure when the surface longitudinal stress maximum exceeds the threshold value $\sigma_r^{max} = 1$ MPa, shown on Figure 6a. The critical undercut length at which this occurs, u_r , can be obtained by inverting the equation

$$\sigma_r^{max} = \frac{6}{H^2} \left[(M - Q\lambda) \sin\left(\frac{x_0}{\lambda}\right) - M \cos\left(\frac{x_0}{\lambda}\right) \right] \exp\left(\frac{x_0}{\lambda}\right) \quad (10)$$

for the undercut length u (see also Equations 3 and 5). Since all of M , Q , and x_0 are functions of u , this cannot in general be done analytically, but it is a very quick numerical calculation. The critical linear undercut length at which rotational failure occurs for an ice thickness of 500 m and varying water depth is shown in Figure 6c, and increases non-linearly with water depth to reach 400 m when the glacier is at flotation. Meanwhile, the location of the stress maximum moves closer to the grounding line for larger water depths. The total calving length measured at the glacier surface l is the sum of the undercut length and the distance to the stress maximum and has a complex form, but is roughly 600 m regardless of water depth (Figure 6c).

Because many tidewater glaciers terminate in water depths that make them close to flotation, it is illuminating to consider these results as a function of ice thickness assuming the glacier is at flotation (Figure 7). In these cases, the glacier always flexes downwards at the terminus. For a given ice thickness, the stress

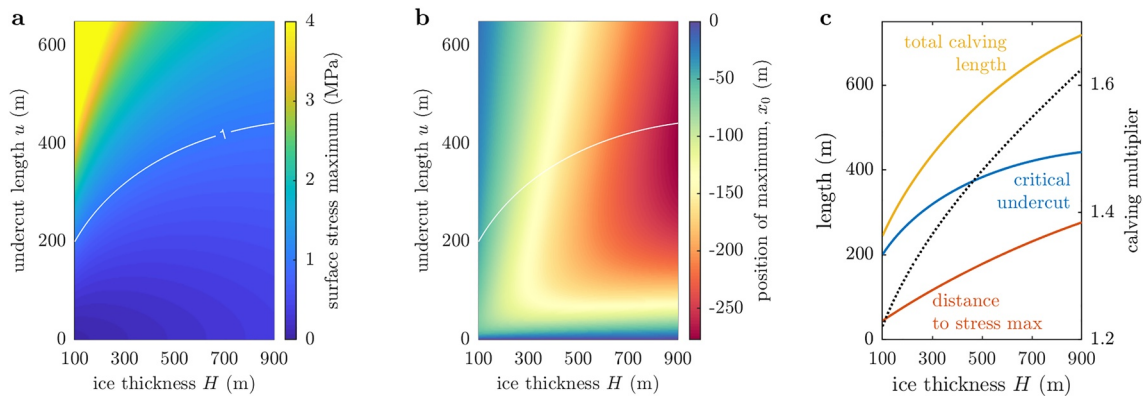


Figure 7. The equivalent of Figure 6, but considered as a function of ice thickness assuming the water depth is such that the glacier is at flotation. (a) Surface longitudinal stress maximum, and (b) position of surface stress maximum. (c) Left axis: the three lengths that determine when and where rotational failure calving occurs, and right axis and black dotted line: the calving multiplier.

maximum increases with the undercut length (Figure 7a). The position of the stress maximum shows a complex dependence on undercut length, first moving upstream from the grounding line then moving back toward the grounding line as undercutting increases (Figure 7b). The position of the stress maximum is much simpler when we consider only its value at the critical undercut length, scaling approximately as $H^{3/4}$ (Figure 7c), as might be expected from the characteristic length λ . The critical undercut length for rotational failure scales approximately as $H^{1/2}$ (Figure 7c), which can be motivated by considering that the right hand side of Equation 10 scales roughly as M/H^2 and M itself scales as Hu^2 based on Equation 9.

Although all of Figures 4–7 show results assuming linear undercutting, we emphasize that the uniformly undercut results are relatively similar, because the depth-integrated torque M and shear Q are not overly sensitive to the choice of undercut shape.

3.5. Dominant Calving-Style

We have argued that serac failure driven by shear stress occurs when the undercut length reaches a critical value given by Equation 8, while rotational failure driven by a high bending moment occurs when the undercut length reaches a critical value given through Equation 10 (Figure 2). The dominant of the two calving styles and the calving multiplier is then determined by which of these critical undercut lengths is reached first, which is in turn determined by the fractional water depth, ice thickness and undercut shape.

An example for a glacier having an ice thickness $H = 500$ m is shown in Figure 8a. With uniform undercutting (Figure 1c), serac failure occurs once the undercut length reaches $u_s = 56$ m (Figure 8a; see also Figure 3). This is smaller than the rotational failure undercut threshold u_r for any water depth, so that in this case, uniform undercutting results only in serac failure. With linear undercutting (Figure 1b), the critical undercut length for serac failure is a function of water depth (Figure 8a). For water depths less than 325 m, the undercut length threshold for serac failure is reached before that for rotational failure. Conversely, for linear undercutting and water depths greater than 325 m, the calving front is relatively stable to serac failure and so rotational failure is the dominant calving-style (Figure 8a). In reality, large glaciers having an ice thickness of 500 m are not found terminating in shallow water because they would be unstable to ice cliff failure (Equation 6). Water depths less than $d = 350$ m are, therefore, unlikely to be observed in reality and only the furthest right portion of Figure 8a is realistic.

This analysis can instead be viewed as a function of ice thickness if a choice of water depth is made; in Figure 8b we choose this to put the terminus at flotation. In this case, there is a clear separation between the critical undercut lengths for serac failure and rotational failure. For all ice thicknesses between 100 and 900 m, the critical undercut length for serac failure is smaller than for rotational failure under uniform undercutting, and larger than for rotational failure under linear undercutting (Figure 8b). Note that the critical undercut length for serac failure differs so markedly between uniform and linear undercutting in large part

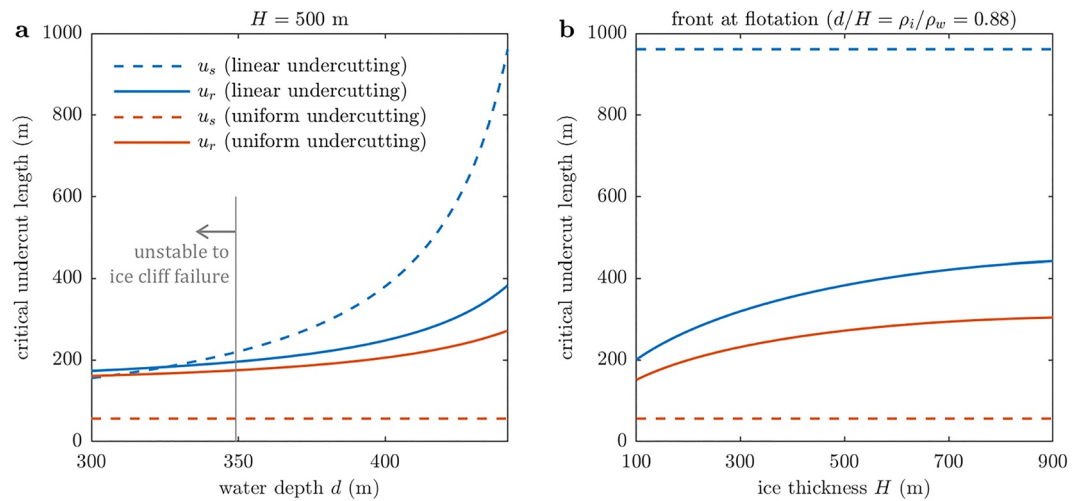


Figure 8. The dependence of calving-style on undercut shape. (a) A fixed ice thickness of $H = 500$ m but variable water depth. The gray dashed line shows the minimum water depth required for the front to be stable to ice cliff failure according to Equation 6. (b) Variable ice thickness, assuming the water depth is such that the front is at flotation.

due to the differing thickness of ice at the grounding line available to support the shear stress (Figure 1 and Equation 7).

Similar results are found when extending the analysis to all ice thickness and fractional water depth combinations that are stable to ice cliff failure (Figure 9). Considering first linear undercutting, for fractional water depths less than 0.5, serac failure dominates for certain ice thicknesses, but otherwise rotational failure is the dominant calving-style (Figure 9a). For fractional water depths greater than 0.5, rotational failure is the dominant calving-style regardless of ice thickness. Because most tidewater glaciers are found to be close to flotation (e.g., Bassis & Walker, 2012), rotational failure will dominate under linear undercutting. In contrast, for uniform undercutting almost all ice thickness and water depth combinations have serac failure as a dominant calving-style, including those stable to ice cliff failure (Figure 9b). Only rather thin glaciers sitting in shallow water undergo rotational failure.

These results can certainly be modified by changing the thresholds for serac and rotational failure (set here at $\sigma_s^{max} = 0.5$ MPa and $\sigma_r^{max} = 1$ MPa), but the sensible choice of these thresholds, together with the

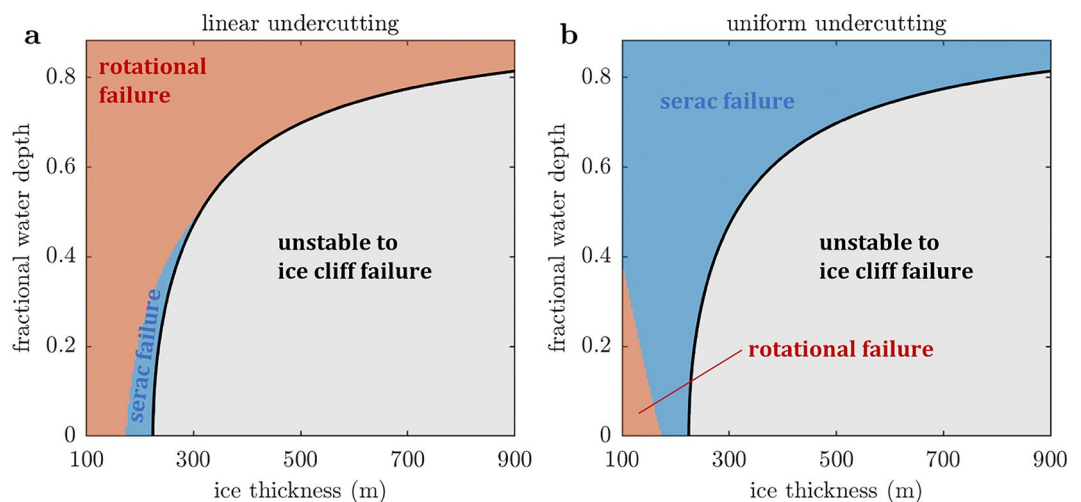


Figure 9. Dominant calving style as a function of fractional water depth and ice thickness for (a) linear undercutting and (b) uniform undercutting.

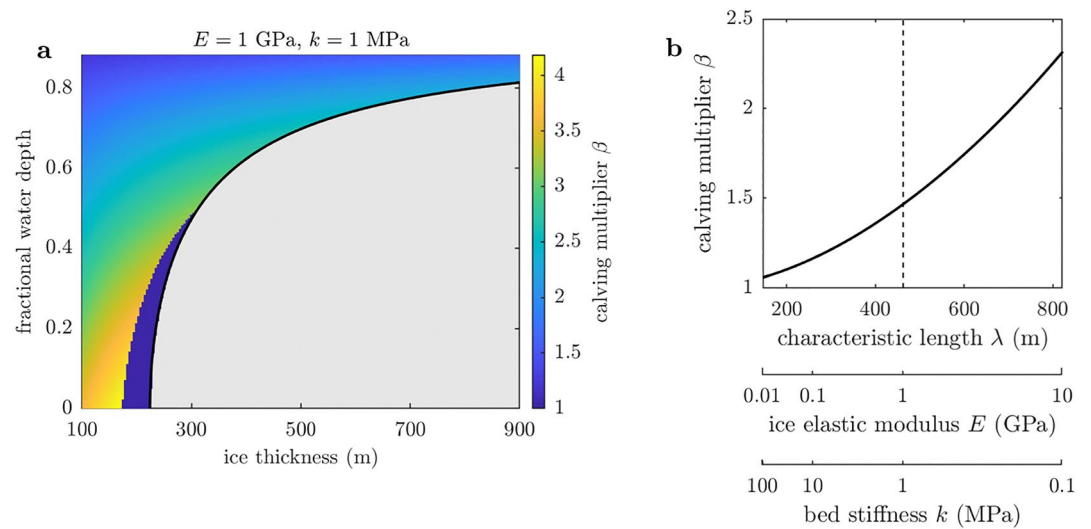


Figure 10. The calving multiplier effect resulting from linear undercutting. The calving multiplier is defined as the ratio of the total calving length (measured at the glacier surface) to the undercut length at the time of calving. (a) Calving multiplier as a function of ice thickness and fractional water depth using the default material parameters for ice and bed strength as throughout the paper. (b) The sensitivity of the calving multiplier to the ice and bed strength, which can also be expressed in terms of the characteristic length. An ice thickness $H = 500 \text{ m}$ at flotation is assumed and the dashed line shows the default parameter values.

clear separation of undercut lengths in Figure 8b and emphatic results in Figure 9, suggests that uniform undercutting intrinsically promotes serac failure while linear undercutting intrinsically promotes rotational failure.

3.6. Calving Multiplier

By considering the dominant calving-style together with the calving position we can analyze the potential for a calving multiplier effect (Figure 2). Under serac failure, the calving position is at the grounding line so that the calving length is equal to the undercut length and the calving multiplier is $\beta = 1$ (i.e., no calving multiplier effect). Under rotational failure, the calving position is upstream of the grounding line, the total calving length exceeds the undercut length and the calving multiplier β exceeds 1 (e.g., Figures 6c and 7c).

Because uniform undercutting is almost exclusively associated with serac failure, there is little potential for a calving multiplier effect under uniform undercutting. Linear undercutting does, however, give a calving multiplier effect whenever rotational failure is the dominant calving-style (Figure 10). The effect is weakest for thin ice close to flotation, when the surface stress maximum is close to the grounding line, and is strongest for thin ice in shallow water (Figures 6c, 7c and 10a). For large glaciers that are close to flotation the calving multiplier takes a value in the range $\beta = 1.4$ to 1.6 (Figures 7c and 10a).

It is important, however, to stress that the magnitude of the calving multiplier is influenced strongly by the material parameters. We have chosen reasonable values, but in a practical application of our results these parameters could be chosen by comparison to observations. An analysis of the sensitivity to the surface stress threshold is given in supporting information; here, we consider the ice and bed strength E and k while holding the stress threshold constant. These parameters influence the position (Equation 5) and, to a lesser extent, the value (Equation 3) of the surface stress maximum through the characteristic length scale λ , which is proportional to $E^{1/4}$ and $k^{-1/4}$. Strengthening the ice (or weakening the bed) by an order of magnitude increases the characteristic length scale by 80%, and for a glacier of thickness 500 m at flotation, increases the calving multiplier by 26% (Figure 10b). Similarly, weakening the ice (or strengthening the bed) by an order of magnitude decreases the characteristic length by 44%, and for the same glacier, decreases the calving multiplier by 9%. As such, the magnitude of the calving multiplier effect is sensitive to the ice and bed strength through their effect on the distance up-glacier over which the terminus effects decay. But, for

glaciers close to flotation, the clear separation between critical undercut lengths for serac and rotational failure (Figure 8b) means that the ice and bed strength do not influence the dominant calving-style.

4. Discussion

4.1. Calving, Undercut Shape, and Submarine Melting

We have derived a metric for serac failure based on depth-mean shear stress at the grounding line and a metric for rotational failure based on the tensile stress at the glacier surface induced by shear and torque at the terminus (Figure 2). Once a choice of stress threshold is made, these metrics give a critical undercut length at which the particular-style of calving occurs. By comparing undercut lengths between failure mechanisms a dominant calving-style emerges, which in turn determines the presence or absence of a calving multiplier effect. We find that the dominant calving-style is critically dependent on the shape of undercutting, with uniform undercutting promoting serac failure and linear undercutting promoting rotational failure.

We have considered only two undercut shapes - linear and uniform (Figure 1)—but clearly many other shapes are possible, including convex or concave undercutting (e.g., Ma & Bassis, 2019), linear or uniform undercutting that does not extend all the way to the fjord surface (e.g., Slater et al., 2017), waterline notching (Petlicki et al., 2015) or overcutting and projecting ice feet (Fried et al., 2019; Wagner et al., 2016). Our calving metrics can be easily generalized to other terminus shapes by appropriate calculation of the depth-integrated torque M and the depth-integrated shear Q (supporting information). In particular, the depth-integrated shear has to compensate for the hydrostatic imbalance of ice beyond the grounding line. For a given undercut length at the bed, therefore, the more ice volume remaining below the water the less likely serac failure is to occur. Uniform undercutting reaching the fjord surface (Figure 1c) is the shape most likely to drive serac failure as it has no ice below the water beyond the grounding line. Linear undercutting (Figure 1b) or uniform undercutting that does not reach the surface both have ice below the water, reducing the hydrostatic imbalance and making larger undercuts more stable to serac failure (e.g., Figure 3).

The sensitivity of calving-style to undercut shape (Figures 8 and 9) then transfers focus to the vertical profile of submarine melting that generates the undercut; submarine melt rate that is uniform with depth will generate uniform undercutting while submarine melt rate that increases with depth will generate linear undercutting. Much work has been undertaken to understand submarine melting and its impact on undercut shape, showing that fjord stratification, subglacial discharge and grounding line depth are all key controls (e.g., Jackson et al., 2020; Jenkins, 2011; Slater et al., 2016; Slater et al., 2017; Sutherland et al., 2019; Xu et al., 2013). We will only highlight one interesting link here in relation to grounding line depth. The highest rates of submarine melting are found in upwelling plumes, generated by the emergence of fresh subglacial discharge from the grounding line, that flush warm water along the terminus (e.g., Mankoff et al., 2016). The height reached by the plume then determines the vertical extent of the region of high submarine melting (De Andrés et al., 2020). At smaller glaciers with shallow grounding lines, the plume is likely to reach the surface, promoting uniform undercutting reaching the fjord surface (Figure 1b; Carroll et al., 2016) and serac failure. At large glaciers with deep grounding lines, the plume is more likely to be trapped in the subsurface, promoting linear undercutting that does not reach the surface (Carroll et al., 2016) and, therefore, rotational failure. As such, the dynamics of submarine melting together with the sensitivity of calving-style to undercut shape may result in contrasts in calving-style between small and large glaciers.

4.2. Parameter Choices and Comparison to Previous Work

Our results are clearly sensitive to the choice of the ice and bed strength and to the two stress thresholds. Bassis and Walker (2012) and Ultee et al. (2020) contain extensive discussions of shear and tensile failure thresholds, respectively. While the values we have adopted are within the ranges used by previous studies, these parameters are also rather idealized notions that assume the ice and bed are perfect and uniform. In reality, the ice will have crevasses and smaller imperfections and inhomogeneities that will reduce the ability of the ice to resist rotational and vertical imbalances. As such, in a real-world application of our results, such as to form a calving parameterization, a pragmatic choice would be to choose the values of these parameters to best match observations. A lack of contemporaneous observations of calving and undercut morphology at tidewater glaciers makes this difficult, but some constraints can be obtained.

Approximately linear undercutting has been observed to reach 350 m at Store Glacier (Rignot et al., 2015) in the presence of a water depth of 500 m and an ice thickness of 570 m (Ryan et al., 2015). Such a degree of undercutting would not be stable within our framework unless $\sigma_s^{max} > 0.2$ MPa and $\sigma_r^{max} > 0.8$ MPa (Figures 3 and 7). The presence of undercutting reaching 220 m at Kangerlussuup Sermia, where the water depth is approximately 250 m and the ice thickness 300 m (Fried et al., 2019) places similar bounds on the stress thresholds. The additional assertion of Fried et al. (2019) that the dominant calving-style at Kangerlussuup Sermia is serac failure suggests that the shear stress threshold is smaller than the tensile failure threshold. One very important point to note in comparing our framework to real glaciers is that we have not accounted for across-glacier bridging stresses that could easily play a role in stabilizing undercut regions (Cowton et al., 2019).

Our results compare well with previous particle modeling studies in which calving styles emerge naturally rather than through a choice of a stress metric for calving. Benn, Astrom, et al. (2017) simulated a calving multiplier effect of magnitude $\beta = 1$ to 4.6 for an ice thickness $H = 100$ m, fractional water depths of 0.58–0.88 and linear undercut lengths $u = 5$ –15 m. The magnitude of the calving multiplier effect was found to decrease with deeper water. The results of Benn, Astrom, et al. (2017) are, therefore, consistent with our conclusions on the calving multiplier effect in terms of both magnitude and variability, given appropriate parameter choices (e.g., Figure 10b). Ma and Bassis (2019) suggested that linear undercutting induces a significant calving multiplier effect but uniform undercutting generally reduces the mass of ice that is calved. Lastly, when imposing linear undercutting across the full width of Bowdoin Glacier, van Dongen et al. (2020) predict rotational rather than serac failure. The consistency of our results with all of these studies suggests that the elastic beam approach presented here is a promising avenue for capturing calving due to melt-undercutting in a computationally efficient manner.

4.3. Limitations and Missing Processes

We have not made much explicit mention of crevasses, yet they are very obviously central to any study on calving. In Section 3.1 we described how the existence of a crevasse would modify the threshold for serac failure and indeed we believe that serac failure would be most likely to occur when a crevasse that is formed upstream is advected across the grounding line. Similarly, the existence of a bending moment in the ice that resists top-forwards rotation would deepen surface crevasses, leaving less ice thickness to support the moment and potentially leading to unstable crevasse growth. In some ways, therefore, rather than considering the inception of crevassing, this study focuses on quantifying whether the overall geometry of the terminus is conducive to the unstable growth of existing crevasses that leads to calving.

A factor not accounted for in this study is ice mélange. It has been suggested that the backstress induced on a glacier terminus by icebergs and sea-ice could be sufficient to suppress calving (Amundson et al., 2010; Burton et al., 2018; Krug et al., 2015; Todd et al., 2018). This suppression could occur by lowering the depth-mean force imbalance at the terminus, thereby reducing longitudinal stretching in the ice. Since mélange is located at or close to the fjord surface, however, the mélange will also induce a torque on the terminus that opposes the torque resulting from ice and water pressure. As such, mélange could subdue rotational failure and allow a terminus to support greater undercutting. Given a mélange backstress and a range of depths over which it acts on the terminus, it would be simple to incorporate mélange into the depth-integrated torque (Equation 9) and the critical undercut length for rotational failure (Equation 10).

The limitations and caveats of our study are numerous and lie largely in its idealized nature. We have assumed the water depth is fixed and that the ice geometry other than the undercut does not change. In reality, these will evolve in time due to tides, ice dynamics and grounding line advance or retreat; the analysis presented in this study essentially assumes that all processes are paused except for undercutting.

By employing an elastic beam model, we have neglected any viscous response to the loads applied at the terminus. The viscous bending timescale for glaciers has been estimated to lie between 2 months and 21 years (Sayag & Worster, 2013). Given that the time interval between calving events at tidewater glaciers is typically smaller than 2 months (e.g., How et al., 2019; Schild & Hamilton, 2013), treating the glacier response to undercutting as elastic is a reasonable approximation, but it is likely that viscous stresses will play a role.

A related point is that we have neglected longitudinal stresses other than those associated with bending. These additional stresses could influence rotational calving or themselves drive calving independently of glacier bending (e.g., Benn et al., 2007). A more complete treatment of the calving problem could, therefore, seek to characterize calving associated with horizontal imbalance at the same time as the calving driven by rotational and vertical imbalance analyzed in this study.

Lastly, and perhaps most limiting of all, we have neglected across-glacier variability, which is a significant simplification in view of the evidence that lateral stress bridging is likely to provide support to localized undercutting (Cowton et al., 2019; van Dongen et al., 2020).

4.4. Prospects for a Frontal Ablation Parameterization

The quantitative metrics for serac and rotational failure proposed in this study offer a promising step toward parameterization of these calving styles. In the representation of a grounded tidewater glacier in a depth-integrated ice sheet model (e.g., Morlighem et al., 2016), the ice-ocean boundary is at the grounding line ($x = 0$ in Figure 1). It is practical, then, to formulate a frontal ablation parameterization, incorporating the sum of calving and submarine melting, that represents along-flow values at the grounding line.

If the glacier and undercut geometry are such that a glacier undergoes serac failure before rotational failure (Equations 8 and 10, Figure 9), then frontal ablation can be represented as a rate that is equal to the submarine melt rate. If instead the glacier and undercut geometry promotes rotational failure, then by combining with a predicted grounding line submarine melt rate, Equations 5 and 10 give the timing and distance upstream at which calving occurs. Averaged over many calving events, frontal ablation could in this case be represented as a rate equal to the product of the calving multiplier (Figure 10) and the grounding line submarine melt rate.

These calving (or frontal ablation) formulations require only basic inputs such as the ice thickness, water depth, undercut shape and submarine melt rate, together with ice and bed strength parameters, making them suitable for including in large-scale, depth-integrated ice sheet models used for sea level projection. Further work could strengthen these formulations by considering the impact of bed slope, bed friction and ice mélange.

5. Conclusions

We have presented an analytical framework based on elastic beam theory for understanding the impact of submarine melt-undercutting on calving. We have shown that, as undercutting by submarine melting progresses, both the depth-integrated torque and the depth-integrated shear experienced by the terminus increase. Our premise is that serac failure, that is, calving only of ice that is undercut, occurs when the shear stress exceeds a threshold value, or equivalently when the undercut length reaches a critical value (Equation 8). Similarly, we suggest that rotational failure, that is, full-thickness calving of ice upstream from the grounding line, occurs when the tensile stress at the glacier surface resulting from downwards flexure of the glacier exceeds a threshold value, or when the undercut length reaches an equivalent critical value (Equation 10). Within this framework, the dominant calving-style and the presence or absence of the calving multiplier effect is determined by which critical undercut length is shorter and will, therefore, be reached first.

The two critical undercut lengths depend on the ice thickness, water depth and shape of melt-undercutting. As a result, glaciers experiencing uniform undercutting are particularly vulnerable to serac failure and experience no calving multiplier effect. Glaciers experiencing linear undercutting are much more stable to serac failure, but are more vulnerable to rotational failure and can experience a calving multiplier effect whereby submarine melting significantly amplifies calving. As such, the geometry of melt-undercutting determines the presence or absence of the calving multiplier effect. This study provides an intuitive analytical framework to be challenged by further observations and modeling, and a promising step toward the parameterization of melt undercut-driven calving in large-scale, depth-integrated ice sheet models.

Data Availability Statement

Due to the theoretical nature of this work, data were not used, nor created for this research.

Acknowledgments

This work was funded by NERC Award NE/P011365/1 (CALISMO: Calving laws for ice sheet models) to PI Benn and NERC IRF NE/T011920/1 (Next generation projections of sea level contribution and freshwater export from the Greenland ice sheet) to PI Slater. This work received support from the DOMINOS project, a component of the International Thwaites Glacier Collaboration (ITGC). Support from National Science Foundation (NSF: Grant 1738896) and Natural Environment Research Council (NERC: Grant NE/S006605/1). Logistics provided by NSF-U.S. Antarctic Program and NERC-British Antarctic Survey. ITGC Contribution No. ITGC-048.

References

- Åström, J. A., Vallot, D., Schäfer, M., Welty, E. Z., O'Neil, S., Bartholomäus, T. C., et al. (2014). Termini of calving glaciers as self-organized critical systems. *Nature Geoscience*, 7, 874–878. <https://doi.org/10.1038/ngeo2290>
- Amundson, J. M., Fahnestock, M., Truffer, M., Brown, J., Lüthi, M. P., & Motyka, R. J. (2010). Ice mélange dynamics and implications for terminus stability, Jakobshavn Isbrae, Greenland. *Journal of Geophysical Research*, 115, F01005. <https://doi.org/10.1029/2009JF001405>
- Aschwanden, A., Fahnestock, M. A., Truffer, M., Brinkerhoff, D. J., Hock, R., Khroulev, C., et al. (2019). Contribution of the Greenland ice sheet to sea level over the next millennium. *Science Advances*, 5(6), eaav9396. <https://doi.org/10.1126/sciadv.aav9396>
- Bartholomäus, T. C., Larsen, C. F., & O'Neil, S. (2013). Does calving matter? Evidence for significant submarine melt. *Earth and Planetary Science Letters*, 380, 21–30. <https://doi.org/10.1016/j.epsl.2013.08.014>
- Bassis, J. N., & Walker, C. C. (2012). Upper and lower limits on the stability of calving glaciers from the yield strength envelope of ice. *Proceedings of the Royal Society A: Mathematical, Physical and Engineering Sciences*, 468(2140), 913–931. <https://doi.org/10.1098/rspa.2011.0422>
- Benn, D. I., Astrom, J., Zwinger, T., Todd, J., Nick, F. M., Cook, S., et al. (2017). Melt-under-cutting and buoyancy-driven calving from tidewater glaciers: New insights from discrete element and continuum model simulations. *Journal of Glaciology*, 63(240), 691–702. <https://doi.org/10.1017/jog.2017.41>
- Benn, D. I., Cowton, T., Todd, J., & Luckman, A. (2017). Glacier calving in Greenland. *Current Climate Change Reports*, 3, 282–290. <https://doi.org/10.1007/s40641-017-0070-1>
- Benn, D. I., Warren, C. R., & Mottram, R. H. (2007). Calving processes and the dynamics of calving glaciers. *Earth-Science Reviews*, 82(3–4), 143–179. <https://doi.org/10.1016/j.earscirev.2007.02.002>
- Burton, J. C., Amundson, J. M., Cassotto, R., Kuo, C.-C., & Dennin, M. (2018). Quantifying flow and stress in ice mélange, the world's largest granular material. *Proceedings of the National Academy of Sciences*, 115(20), 5105–5110. <https://doi.org/10.1073/pnas.1715136115>
- Carroll, D., Sutherland, D. A., Hudson, B., Moon, T., Catania, G. A., Shroyer, E. L., et al. (2016). The impact of glacier geometry on meltwater plume structure and submarine melt in Greenland fjords. *Geophysical Research Letters*, 43(18), 9739–9748. <https://doi.org/10.1002/2016GL070170>
- Catania, G. A., Stearns, L. A., Moon, T. A., Enderlin, E. M., & Jackson, R. H. (2020). Future evolution of Greenland's marine-terminating outlet glaciers. *Journal of Geophysical Research: Earth Surface*, 125(2). <https://doi.org/10.1029/2018JF004873>
- Cook, S., Rutt, I. C., Murray, T., Luckman, A., Zwinger, T., Selmes, N., et al. (2014). Modelling environmental influences on calving at Helheim Glacier in eastern Greenland. *The Cryosphere*, 8(3), 827–841. <https://doi.org/10.5194/tc-8-827-2014>
- Cowton, T. R., Todd, J. A., & Benn, D. I. (2019). Sensitivity of tidewater glaciers to submarine melting governed by plume locations. *Geophysical Research Letters*, 46(20), 11219–11227. <https://doi.org/10.1029/2019GL084215>
- De Andrés, E., Slater, D. A., Straneo, F., Otero, J., Das, S., & Navarro, F. (2020). Surface emergence of glacial plumes determined by fjord stratification. *The Cryosphere*, 14(6), 1951–1969. <https://doi.org/10.5194/tc-14-1951-2020>
- Fried, M. J., Carroll, D., Catania, G. A., Sutherland, D. A., Stearns, L. A., Shroyer, E. L., & Nash, J. D. (2019). Distinct frontal ablation processes drive heterogeneous submarine terminus morphology. *Geophysical Research Letters*, 46(21), 12083–12091. <https://doi.org/10.1029/2019GL083980>
- Goelzer, H., Nowicki, S., Payne, A., Larour, E., Seroussi, H., Lipscomb, W. H., & van den Broeke, M. (2020). The future sea-level contribution of the Greenland ice sheet: A multi-model ensemble study of ISMIP6. *The Cryosphere*, 14(9), 3071–3096. <https://doi.org/10.5194/tc-2019-319>
- Hanson, B., & Hooke, R. L. (2000). Glacier calving: A numerical model of forces in the calving-speed/water-depth relation. *Journal of Glaciology*, 46(153), 188–196. <https://doi.org/10.3189/172756500781832792>
- Hock, R., Bliss, A., Marzeion, B., Giesen, R. H., Hirabayashi, Y., Huss, M., et al. (2019). GlacierMIP – A model intercomparison of global-scale glacier mass-balance models and projections. *Journal of Glaciology*, 65(251), 453–467. <https://doi.org/10.1017/jog.2019.22>
- How, P., Schild, K. M., Benn, D. I., Noormets, R., Kirchner, N., Luckman, A., et al. (2019). Calving controlled by melt-under-cutting: Detailed calving styles revealed through time-lapse observations. *Annals of Glaciology*, 60(78), 20–31. <https://doi.org/10.1017/aog.2018.28>
- Hughes, T. (1992). Theoretical calving rates from glaciers along ice walls grounded in water of variable depths. *Journal of Glaciology*, 38(129), 282–294. <https://doi.org/10.3189/S0022143000003695>
- Jackson, R. H., Nash, J. D., Kienholz, C., Sutherland, D. A., Amundson, J. M., Motyka, R. J., et al. (2020). Meltwater intrusions reveal mechanisms for rapid submarine melt at a tidewater glacier. *Geophysical Research Letters*, 47(2), e2019GL085335. <https://doi.org/10.1029/2019GL085335>
- Jenkins, A. (2011). Convection-driven melting near the grounding lines of ice shelves and tidewater glaciers. *Journal of Physical Oceanography*, 41(12), 2279–2294. <https://doi.org/10.1175/JPO-D-11-03.1>
- Krug, J., Durand, G., Gagliardini, O., & Weiss, J. (2015). Modelling the impact of submarine frontal melting and ice mélange on glacier dynamics. *The Cryosphere*, 9, 989–1003. <https://doi.org/10.5194/tc-9-989-2015>
- Luckman, A., Benn, D. I., Cottier, F., Bevan, S., Nilsen, F., & Inall, M. (2015). Calving rates at tidewater glaciers vary strongly with ocean temperature. *Nature Communications*, 6, 8566. <https://doi.org/10.1038/ncomms9566>
- Ma, Y., & Bassis, J. N. (2019). The effect of submarine melting on calving from marine terminating glaciers. *Journal of Geophysical Research: Earth Surface*, 124(2), 334–346. <https://doi.org/10.1029/2018JF004820>
- Mankoff, K. D., Straneo, F., Cenedese, C., Das, S. B., Richards, C. G., & Singh, H. (2016). Structure and dynamics of a subglacial discharge plume in a Greenlandic fjord. *Journal of Geophysical Research: Oceans*, 121(12), 8670–8688. <https://doi.org/10.1002/2016JC011764>
- Mercenier, R., Lüthi, M. P., & Vieli, A. (2020). How oceanic melt controls tidewater glacier evolution. *Geophysical Research Letters*, 47(8), e2019GL086769. <https://doi.org/10.1029/2019GL086769>
- Morlighem, M., Bondzio, J., Seroussi, H., Rignot, E., Larour, E., Humbert, A., & Rebuffi, S. (2016). Modeling of Store Gletscher's calving dynamics, West Greenland, in response to ocean thermal forcing. *Geophysical Research Letters*, 43(6), 2659–2666. <https://doi.org/10.1002/2016GL067695>
- Morlighem, M., Wood, M., Seroussi, H., Choi, Y., & Rignot, E. (2019). Modeling the response of northwest Greenland to enhanced ocean thermal forcing and subglacial discharge. *The Cryosphere*, 13(2), 723–734. <https://doi.org/10.5194/tc-13-723-2019>

- Mosbeux, C., Wagner, T. J. W., Becker, M. K., & Fricker, H. A. (2020). Viscous and elastic buoyancy stresses as drivers of ice-shelf calving. *Journal of Glaciology*, 66(258), 643–657. <https://doi.org/10.1017/jog.2020.35>
- O'Leary, M., & Christoffersen, P. (2013). Calving on tidewater glaciers amplified by submarine frontal melting. *The Cryosphere*, 7(1), 119–128. <https://doi.org/10.5194/tc-7-119-2013>
- Petlicki, M., Cieply, M., Jania, J. A., Prominska, A., & Kinnard, C. (2015). Calving of a tidewater glacier driven by melting at the waterline. *Journal of Glaciology*, 61(229), 851–863. <https://doi.org/10.3189/2015JG15J062>
- Rignot, E., Fenty, I., Xu, Y., Cai, C., & Kemp, C. (2015). Undercutting of marine-terminating glaciers in West Greenland. *Geophysical Research Letters*, 42(14), 5909–5917. <https://doi.org/10.1002/2015GL064236>
- Ryan, J. C., Hubbard, A. L., Box, J. E., Todd, J., Christoffersen, P., Carr, J. R., et al. (2015). UAV photogrammetry and structure from motion to assess calving dynamics at Store Glacier, a large outlet draining the Greenland ice sheet. *The Cryosphere*, 9(1), 1–11. <https://doi.org/10.5194/tc-9-1-2015>
- Sayag, R., & Worster, M. G. (2011). Elastic response of a grounded ice sheet coupled to a floating ice shelf. *Physical Review E*, 84(3), 036111. <https://doi.org/10.1103/PhysRevE.84.036111>
- Sayag, R., & Worster, M. G. (2013). Elastic dynamics and tidal migration of grounding lines modify subglacial lubrication and melting. *Geophysical Research Letters*, 40(22), 5877–5881. <https://doi.org/10.1002/2013GL057942>
- Schild, K. M., & Hamilton, G. S. (2013). Seasonal variations of outlet glacier terminus position in Greenland. *Journal of Glaciology*, 59(216), 759–770. <https://doi.org/10.3189/2013JG12J238>
- Sergienko, O. V. (2010). Elastic response of floating glacier ice to impact of long-period ocean waves. *Journal of Geophysical Research*, 115(F4). <https://doi.org/10.1029/2010JF001721>
- Seroussi, H., Nowicki, S., Payne, A. J., Goelzer, H., Lipscomb, W. H., Abe Ouchi, A., & Zwinger, T. (2020). ISMIP6 Antarctica: A multi-model ensemble of the Antarctic ice sheet evolution over the 21st century. *The Cryosphere*, 14(9), 3033–3070. <https://doi.org/10.5194/tc-2019-324>
- Shapiro, D. N., Joughin, I. R., Poinar, K., Morlighem, M., & Gillet-Chaulet, F. (2016). Basal resistance for three of the largest Greenland outlet glaciers. *Journal of Geophysical Research: Earth Surface*, 121(1), 168–180. <https://doi.org/10.1002/2015JF003643>
- Slater, D. A., Goldberg, D. N., Nienow, P. W., & Cowton, T. R. (2016). Scalings for submarine melting at tidewater glaciers from buoyant plume theory. *Journal of Physical Oceanography*, 46(6), 1839–1855. <https://doi.org/10.1175/JPO-D-15-0132.1>
- Slater, D. A., Nienow, P. W., Goldberg, D. N., Cowton, T. R., & Sole, A. J. (2017). A model for tidewater glacier undercutting by submarine melting. *Geophysical Research Letters*, 44(5), 2360–2368. <https://doi.org/10.1002/2016GL072374>
- Slater, D. A., Straneo, F., Das, S. B., Richards, C. G., Wagner, T. J. W., & Nienow, P. W. (2018). Localized plumes drive front-wide ocean melting of a Greenlandic tidewater glacier. *Geophysical Research Letters*, 45(22), 12350–12358. <https://doi.org/10.1029/2018GL080763>
- Slater, D. A., Straneo, F., Felikson, D., Little, C. M., Goelzer, H., Fettweis, X., & Holte, J. (2019). Estimating Greenland tidewater glacier retreat driven by submarine melting. *The Cryosphere*, 13(9), 2489–2509. <https://doi.org/10.5194/tc-13-2489-2019>
- Straneo, F., & Heimbach, P. (2013). North Atlantic warming and the retreat of Greenland's outlet glaciers. *Nature*, 504, 36–43. <https://doi.org/10.1038/nature12854>
- Sutherland, D. A., Jackson, R. H., Kienholz, C., Amundson, J. M., Dryer, W. P., Duncan, D., et al. (2019). Direct observations of submarine melt and subsurface geometry at a tidewater glacier. *Science*, 365(6451), 369–374. <https://doi.org/10.1126/science.aax3528>
- The IMBIE Team. (2020). Mass balance of the Greenland ice sheet from 1992 to 2018. *Nature*, 579, 233–239. <https://doi.org/10.1038/s41586-019-1855-2>
- Todd, J., & Christoffersen, P. (2014). Are seasonal calving dynamics forced by buttressing from ice mélange or undercutting by melting? Outcomes from full-Stokes simulations of Store glacier, West Greenland. *The Cryosphere*, 8(6), 2353–2365. <https://doi.org/10.5194/tc-8-2353-2014>
- Todd, J., Christoffersen, P., Zwinger, T., Råback, P., & Benn, D. I. (2019). Sensitivity of a calving glacier to ice–ocean interactions under climate change: New insights from a 3-D full-Stokes model. *The Cryosphere*, 13(6), 1681–1694. <https://doi.org/10.5194/tc-13-1681-2019>
- Todd, J., Christoffersen, P., Zwinger, T., Raback, P., Chauche, N., Benn, D., et al. (2018). A full-stokes 3D calving model applied to a large Greenlandic glacier. *Journal of Geophysical Research: Earth Surface*, 123(3), 410–432. <https://doi.org/10.1002/2017JF004349>
- Ultee, L., Meyer, C., & Minchew, B. (2020). Tensile strength of glacial ice deduced from observations of the 2015 eastern Skaftá cauldron collapse, Vatnajökull ice cap, Iceland. *Journal of Glaciology*, 66, 1024–1033. <https://doi.org/10.1017/jog.2020.65>
- Vallot, D., Åström, J., Zwinger, T., Pettersson, R., Everett, A., Benn, D. I., et al. (2018). Effects of undercutting and sliding on calving: A global approach applied to Kronebreen, Svalbard. *The Cryosphere*, 12(2), 609–625. <https://doi.org/10.5194/tc-12-609-2018>
- van den Broeke, M. R., Enderlin, E. M., Howat, I. M., Kuipers Munneke, P., Noel, B. P. Y., Berg, van de, W. J., et al. (2016). On the recent contribution of the Greenland ice sheet to sea level change. *The Cryosphere*, 10(5), 1933–1946. <https://doi.org/10.5194/tc-10-1933-2016>
- van Dongen, E. C. H., Åström, J. A., Jouvett, G., Todd, J., Benn, D. I., & Funk, M. (2020). Numerical modeling shows increased fracturing due to melt-undercutting prior to major calving at Bowdoin Glacier. *Frontiers in Earth Science*, 8, 253. <https://doi.org/10.3389/feart.2020.00253>
- Vaughan, D. G. (1995). Tidal flexure at ice shelf margins. *Journal of Geophysical Research: Solid Earth*, 100(B4), 6213–6224. <https://doi.org/10.1029/94JB02467>
- Wagner, T. J. W., James, T. D., Murray, T., & Vella, D. (2016). On the role of buoyant flexure in glacier calving. *Geophysical Research Letters*, 43(1), 232–240. <https://doi.org/10.1002/2015GL067247>
- Wagner, T. J. W., Straneo, F., Richards, C. G., Slater, D. A., Stevens, L. A., Das, S. B., & Singh, H. (2019). Large spatial variations in the flux balance along the front of a Greenland tidewater glacier. *The Cryosphere*, 13(3), 911–925. <https://doi.org/10.5194/tc-13-911-2019>
- Xu, Y., Rignot, E., Fenty, I., Menemenlis, D., & Flexas, M. M. (2013). Subaqueous melting of Store Glacier, West Greenland from three-dimensional, high-resolution numerical modeling and ocean observations. *Geophysical Research Letters*, 40(17), 4648–4653. <https://doi.org/10.1002/grl.50825>